Modeling wave propagation in realistic heart geometries using the phase-field method

Flavio H. Fenton
Department of Physics, Hofstra University, Hempstead, New York 11549 and Beth Israel Medical Center, New York, New York 10003

Elizabeth M. Cherry
Department of Physics, Hofstra University, Hempstead, New York 11549

Alain Karma
Department of Physics, Northeastern University, Boston, Massachusetts 02115

Wouter-Jan Rappel
Department of Physics, University of California, San Diego, La Jolla, California 92093

(Received 23 June 2004; accepted 3 November 2004; published online 4 February 2005)

We present a novel algorithm for modeling electrical wave propagation in anatomical models of the heart. The algorithm uses a phase-field approach that represents the boundaries between the heart muscle and the surrounding medium as a spatially diffuse interface of finite thickness. The chief advantage of this method is to automatically handle the boundary conditions of the voltage in complex geometries without the need to track the location of these boundaries explicitly. The algorithm is shown to converge accurately in nontrivial test geometries with no-flux (zero normal current) boundary conditions as the width of the diffuse interface becomes small compared to the width of the cardiac action potential wavefront. Moreover, the method is illustrated for anatomically realistic models of isolated rabbit and canine ventricles as well as human atria. © *2005 American Institute of Physics*. [DOI: 10.1063/1.1840311]

The mechanisms for the generation and maintenance of cardiac arrhythmias, the leading cause of death in the industrialized world, are poorly understood. Computer modeling can furnish valuable information, provided that the models used are sufficiently realistic. Modeling electrical wave propagation in models of cardiac geometries requires not only an accurate description of the electrophysiological properties of the heart but also a precise implementation of the geometrical structure and fiber orientation within the tissue. This paper addresses these geometrical requirements and presents a new algorithm to model wave propagation in anatomical models of the heart. The algorithm is based on the diffuse interface phase-field approach that has been used in a wide range of contexts. Simulation results are presented that quantify the accuracy of the method and illustrate its application to realistic heart geometries ranging from rabbit and canine ventricles to the human atria.

I. INTRODUCTION

Despite intense research over the past decades, the precise mechanisms for the onset and maintenance of fibrillation remain poorly understood. Reentrant excitations, which occur when the propagation of the electric wave is blocked in some directions,[1,2] causing the wave front to curl and reenter previously excited tissue, are thought to play an important role in many cases.[3–5] Computer models are important tools in the analysis of arrhythmia mechanisms because, unlike most experiments, simulations can easily provide information on both surface and interior activity. However, most computational studies of reentrant arrhythmias have been performed in simplified domains to focus on understanding reentry as a function of electrophysiological parameters using various existing models of cardiac cell membrane dynamics.[6–9] Nevertheless, it is being increasingly recognized that understanding the evolution of cardiac arrhythmias requires analyzing the role of anatomy as well. For example, numerical studies have shown that the anisotropic fiber rotation of the ventricles can alter the orientation of reentrant waves[10] and can even destabilize them.[11–13] Similarly, periodic boundary conditions[9] and surface curvature[14] can complicate reentry in some cases.

Numerical modeling of reentrant arrhythmias using realistic three-dimensional cardiac geometries and ionic cell models has become increasingly feasible due to rapid advances in computer power. The earliest simulations of electrical activity in realistic heart structures in the 1960s combined cellular automata using varying degrees of coarseness with structures extrapolated from published cross sections of canine hearts (216 elements)[15] and, later, digitized from a human heart (27 000 3 mm cubic blocks).[16] Increasing levels of complexity have been added to simulations using realistic cardiac anatomy with the incorporation of anisotropy,[17] the replacement of cellular automata with ionic cell models,[18] and the use of data sets with fiber orientations obtained from high-resolution dissections of canine[19] and rabbit[20] ventricles.[14,21–23] Harrild and Henriquez have also developed and used a realistic structural and electrophysiological model of human atria.[24]

The use of anatomical models of the heart requires the accurate solution of boundary conditions on the voltage in complex shapes, e.g., a no-flux (zero normal current) boundary condition in the simplest case where the heart is isolated. In finite-difference algorithms, this major difficulty has been overcome so far by defining additional external grid points. The values of these ghost points are then determined in the most convenient manner.[21,23] An undesirable feature of this approach, however, is that it is possible for the same ghost cell to have different values depending on which neighboring cell is being updated. Note, however, that it is possible to implement a finite-difference scheme with only interior grid points using a recently introduced immersed interface method with fiber anisotropy in two[25] and three dimensions.[26] Another commonly used technique, finite-element methods, is able to handle nonflux boundary conditions naturally.[14,22,27] However, these methods are generally slower than finite differences for equivalent grid spacings and are more cumbersome to implement.

The purpose of this paper is to present a new algorithm that accurately implements no-flux boundary conditions in arbitrary geometries, and which can, therefore, be used to model wave propagation in realistic models of cardiac anatomy. Our algorithm is based on the phase-field approach that has been applied successfully to a wide variety of problems including dendritic solidification,[28] viscous fingering,[29] crack propagation,[30,31] the tumbling of vesicles[32] and intracellular dynamics.[33] This method has the chief advantage that it avoids the need to track the interface explicitly by introducing an auxiliary field that makes the interface spatially diffuse. This procedure introduces a new length scale, the interface width. Therefore, results are fully converged only if they are independent of this width for sufficiently thin interfaces. This paper will demonstrate that it is computationally feasible to achieve this convergence using a simple finite-difference discretization of the continuous propagation models. Here, we use this approach to model only fixed geometries with stationary boundaries but, in principle, it can be extended to model moving boundaries. This extension appears very promising to model the full electromechanically contracting heart by coupling the dynamics of the phase field to the displacement field in order to include the effect of contractile forces, as well as to model blood flow in the exterior domain.

The paper is organized as follows. In Sec. II we introduce the phase-field method and discuss the equations governing the electrical activity. In Sec. III we quantify the accuracy of our method through the investigation of electrical wave propagation in nontrivial geometries. In Sec. IV we present results of simulations using models of rabbit ventricles, canine ventricles and human atria. Finally, Sec. V contains our conclusions and a discussion of some future extensions.

II. METHODS

The dynamics of the transmembrane potential V (mV) is given by the standard continuous cable equation:[34]

$$C_m \frac{\partial V}{\partial t} = \nabla \cdot \frac{\sigma}{S_v} \nabla V - I_{\text{ion}}, \tag{1}$$

where C_m (μF cm^{-2}) is the membrane capacitance, ∇ is the gradient operator, I_{ion} (μA cm^{-2}) is the total membrane ionic current, σ is the conductivity tensor, and S_v is the surface to volume ratio. It is also convenient to define the anisotropic diffusion tensor $\mathbf{D}=\sigma/(S_v C_m)$, whose $d\times d$ elements (where d is the dimension of space) depend on the local fiber orientation that generally varies in space in the heart.

For an isolated tissue, there is zero current flow normal to the tissue boundaries:

$$\mathbf{n}\cdot\mathbf{D}\nabla V = 0, \tag{2}$$

where $\mathbf{n}$ is the unit vector normal to the heart surface. Note that this boundary condition only reduces to the standard Neumann boundary condition $\mathbf{n}\cdot\nabla V=0$ when diffusion is isotropic. The term "no-flux" is often associated with this Neumann boundary condition. It is used here, however, to refer to the more general boundary condition of Eq. (2) with the interpretation that it corresponds to no current flux normal to the boundary. To date, most numerical studies of cardiac wave propagation have focused on simplified geometries including two-dimensional sheets and three-dimensional slabs of tissue (see., e.g., Refs. 6–9). For these simplified geometries, it is straightforward to implement no-flux boundary conditions, even when including tissue anisotropy. For example, in a slab of tissue, anisotropy can be incorporated easily when the tissue fibers are parallel to faces of the slab.[11,12,35] In contrast, hearts have much more complicated geometries that include curved boundaries and complicated fiber orientations.[36]

To treat irregular geometries using the phase-field methodology, we introduce an auxiliary field ϕ that takes on different values inside and outside cardiac tissue and varies smoothly across a thin diffusive interface connecting these two regions. Here, we choose for simplicity $\phi=1$ in the interior of the heart and $\phi=0$ in the exterior of the heart.

As has been shown in various applications of the phase-field method,[28,37] the precise form of the phase-field profile in the thin interface region is not critical to the algorithm. In this paper, we have chosen to calculate the phase field via a relaxation method. For this, the heart is placed in a computational box that can accommodate its size. In the interior and the exterior of the heart, ϕ is initially set to 1 and 0, respectively. The smooth values of ϕ, which are to be used later in wave propagation simulations, are then determined by solving the equation

$$\frac{\partial \phi}{\partial t} = \xi^2 \nabla^2 \phi - \frac{\partial G(\phi)}{\partial \phi}, \tag{3}$$

where ξ is a parameter that controls the width of the interface and the function $G(\phi)$ has the form of a double-well potential with minima at $\phi=0$ and $\phi=1$. Therefore, it attempts to maintain ϕ at the values 1 and 0 in the interior and exterior regions, respectively, whereas the diffusion operator tends to smooth out the spatial discontinuity of ϕ at the boundary between these two regions. The balance between these two terms creates a spatially diffuse interface with a width that

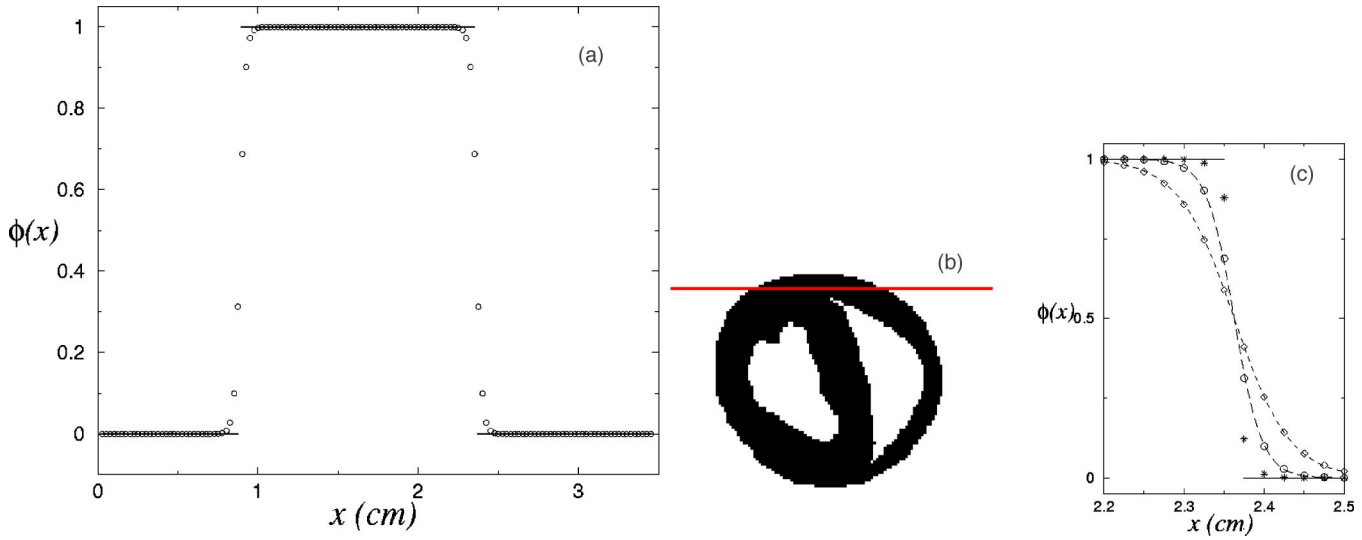

FIG. 1. (Color online). (a) Example of the phase field ϕ along a one-dimensional section from the slice of rabbit ventricles shown in (b). The solid line indicates the original values of 1 or 0 assigned to ϕ and the open circles represent the final steady-state values of ϕ after solving Eq. (3) using $\xi=0.05$ cm. (c) Different solutions for ϕ using $\xi=0.075$, 0.05, and 0.025 cm corresponding to diamonds, circles and stars, respectively. Note that for the choice of G in Eq. (3), ϕ matches $(1+\tanh((2.3625-x)/\xi))/2$, as shown by the long dashed curve when using $\xi=0.05$ cm and the short dashed curve when using $\xi=0.075$ cm. The width of the interface is approximately 4ξ.

depends on the control parameter ξ. For the standard form of a double-well potential,

$$G(\phi) = -\frac{(2\phi-1)^2}{4} + \frac{(2\phi-1)^4}{8}, \tag{4}$$

the one-dimensional solution of ϕ across the interface in an infinite domain is given by

$$\phi(x) = \tfrac{1}{2} + \tfrac{1}{2}\tanh((a-x)/\xi), \tag{5}$$

which corresponds to an interface centered at $x=a$ [i.e., where $\phi(a)=1/2$]. Note that Eq. (3) can be written in the variational form $\partial\phi/\partial t=-\delta\mathcal{F}/\delta\phi$, where $\mathcal{F}$ is the Lyapunov functional $\mathcal{F}=\int dV[\xi^2|\nabla\phi|^2/2+G(\phi)]$; $\int dV$ denotes the spatial integral over the whole computational volume. As long as there are no fluxes across boundaries at infinity, the Lyapunov functional decreases monotonically with time $(d\mathcal{F}/dt\leqslant 0)$.

In practice, our domains have finite extent, and iterating Eq. (3) with initial values of ϕ as described above can lead to the filling of anatomical voids: subdomains where the initial condition is $\phi=0$ can be replaced by $\phi=1$. Thus, we integrate Eq. (3) until a reasonably smooth interface has been created. Typically, we used a time step of $\Delta t=0.01$ ms and a spatial discretization of $\Delta x=0.025$ cm. An example of this integration performed on an arbitrary line across a slice of a rabbit ventricular structure[20] using $\xi=0.05$ cm is shown in Fig. 1. The width of the diffusive interface is approximately 4ξ, as can be seen in Fig. 1(c), which shows the phase field for three different values of ξ. As explained below, the value of ξ controls the error in the algorithm.

The calculated stationary profile of ϕ is used to interpolate smoothly between the electrical properties of the interior and exterior regions. Because the membrane capacitance, the membrane current, and the conductivity vanish in the exterior domain, the simplest interpolation consists of making the substitutions $C_m\rightarrow\phi C_m$, $I_{\text{ion}}\rightarrow\phi I_{\text{ion}}$, and $\sigma\rightarrow\phi\sigma$ in Eq. (1), respectively. After dividing both sides by C_m, this equation can then be rewritten in the following form:

$$\phi\frac{\partial V}{\partial t} = \nabla\cdot[\mathbf{D}\phi\nabla V] - \phi\frac{I_{\text{ion}}}{C_m}. \tag{6}$$

To show that this extension can correctly incorporate the boundary conditions, we consider for simplicity a one-dimensional domain with a boundary at $x=a$ as illustrated in Fig. 1(c). Integrating Eq. (6) over the boundary yields

$$D\left.\frac{\partial V}{\partial x}\right|_{x=a-\xi} \approx -\int_{a-\xi}^{a+\xi} dx\phi\left[\frac{\partial V}{\partial t}+\frac{I_{\text{ion}}}{C_m}\right], \tag{7}$$

since $\phi(a-\xi)\approx 1$ and $\phi(a+\xi)\approx 0$. If we neglect the spatial variation of the right-hand side of Eq. (7), we find

$$\left.\frac{\partial V}{\partial x}\right|_{x=a} \sim F\xi, \tag{8}$$

where the prefactor F is discussed below. Thus, in the so-called sharp interface limit $\xi\rightarrow 0$, the no-flux boundary condition is recovered. In addition, Eq. (6) reduces to Eq. (1) in the interior of the heart where $\phi=1$.

Note that the elements of the diffusion tensor, or equivalently the three components (f^x, f^y, f^z) of the fiber orientation from which these elements can be calculated, are only known in an anatomical heart model at the points in the interior and on the surface of the tissue where $\phi=1$ originally, before ϕ is relaxed using Eq. (3), as shown for representative slices in Figs. 2(a) and 2(b). To solve Eq. (6), however, these elements must be obtained for points inside the diffuse interface region that lie in the exterior region where ϕ was originally zero and where no fiber information exists. Fiber orientations at these points are obtained in an iterative manner. In each iteration, fiber information is determined for all points which have at least one neighbor with fiber orien-

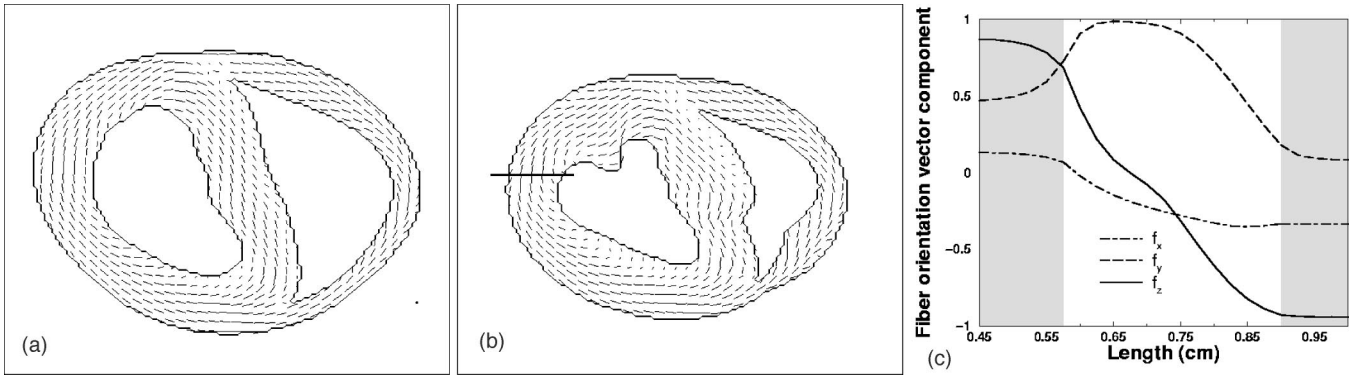

FIG. 2. (Color online). Fiber orientation information for the anatomical model of rabbit ventricles of Ref. 20. (a) and (b) Slices 2 cm (a) and 1.5 cm (b) from the apex showing the projections of the three-dimensional fibers in the $x-y$ plane. (c) The three components of the fiber orientation vectors along the line in (b) for points inside the original domain (white area, length between 0.57 and 0.9 cm) and points in the enlarged domain (gray areas) whose fiber values originally were undefined. Continuity is present in all components. See text for details of the iterative process used to determine values for previously undefined fiber orientations.

tation values and whose fiber orientations are not yet defined by averaging the values of each fiber direction component f^x, f^y, and f^z for all neighbors with defined values and normalizing the resultant vector. The iterative process is continued until all points in the enlarged domain have fiber information. Figure 2(c) shows the three components of both the originally defined (white area) and the iteratively obtained (gray area) fiber orientation vectors and demonstrates continuity in fiber direction.

It is important to note that our algorithm is independent of the discretization and integration method used to solve Eq. (6) numerically.[37] In this paper, we use a finite-difference scheme with a uniform spacing Δx. The time integration is carried out with an explicit Euler method. For clarity of exposition, we describe the algorithm in one dimension and reserve the details of the implementation in higher dimensions for Appendix A. The governing equation can be written without the local ionic current terms as $\phi(dV/dt)=\partial J/\partial x$, where $J=D\phi(\partial V/\partial x)$ is a flux. We calculate the derivative of this flux on a mesh with nodes that are on the midpoints of the lines connecting the gridpoints. Thus, for gridpoint i, the derivative of the flux is written as

$$\frac{\partial J^i}{\partial x}=\frac{J^{i+1/2}-J^{i-1/2}}{\Delta x}. \tag{9}$$

In this expression, $J^{i+1/2}$ can be written as

$$\frac{1}{2}((D\phi)^i+(D\phi)^{i+1})\frac{V^{i+1}-V^i}{\Delta x}, \tag{10}$$

where we have taken the average of the product $D\phi$ as the value at the midpoint. Combined with a similar expression for $J^{i-1/2}$, a finite-difference scheme can be obtained and expressed as

$$\phi^i\frac{dV^i}{dt}=F^i(i-1)V^{i-1}+F^i(i)V^i+F^i(i+1)V^{i+1}, \tag{11}$$

where the prefactors $F^m(n)$ are functions of the phase field and the diffusion tensor using terms at point n to calculate values for point m. This discretization scheme, together with the fact that the phase field approaches 0 at the edges of the computation box, ensures that $\int \phi V\, d\vec{x}$ is conserved. For the full three-dimensional (3D) simulations, this procedure includes the other two directions, taking into account the cross-derivatives to incorporate the anisotropic nature of the tissue. This results in an expression for the time derivative of $V^{i,j,k}$ that is a weighted average of its 6 nearest neighbors, its 12 next-nearest neighbors and itself. Explicit expressions for these weights are given in Appendix A. Because the fiber orientation changes from point to point, these weights must be calculated for each point in the tissue, but these weighting values can be computed once and stored in memory using 19 three-dimensional matrices.

Because the values of the phase field away from the heart surface approach zero exponentially on a scale $\sim\xi$, it is not necessary to solve Eq. (6) over the whole computational domain. In practice, no calculations are performed below a cut-off value for ϕ close to zero, which results in a substantial computational saving. We have verified that no significant alterations in the solution or wave propagation speed occur for cut-off values of $\phi=1\times10^{-4}$ or smaller when using $\xi=0.025$ cm (the cut-off value should be decreased as ξ is reduced). For our typical choices of ξ, Δx, and the value of the cutoff an average of roughly three to four relevant gridpoints are added to the actual domain in the direction normal to the surface.

For the descriptions of the ionic currents I_{ion} in Eq. (1), a wide range of models with varying degrees of detail and complexity can be used. To show that the phase-field method can be used for a variety of models, we use here two recent ionic models, the Nygren *et al.* human atrial model[38] and the Fox *et al.* canine ventricular model,[39] shown in Figs. 3(a) and 3(b), respectively. In addition, we use a four-variable phenomenological model with intermediate detail[12] whose parameters can be varied to reproduce the action potential and rate adaptations obtained in experiments and in detailed ionic models.[9,40,41] In this paper, parameters are set to reproduce action potentials similar to experimental recordings of canine epicardial cells [see Fig. 3(c)] while producing a different maximum upstroke velocity than the Fox *et al.* model [see Fig. 3(a)], thereby allowing analysis of the effect of upstroke steepness on the accuracy of the phase-field method

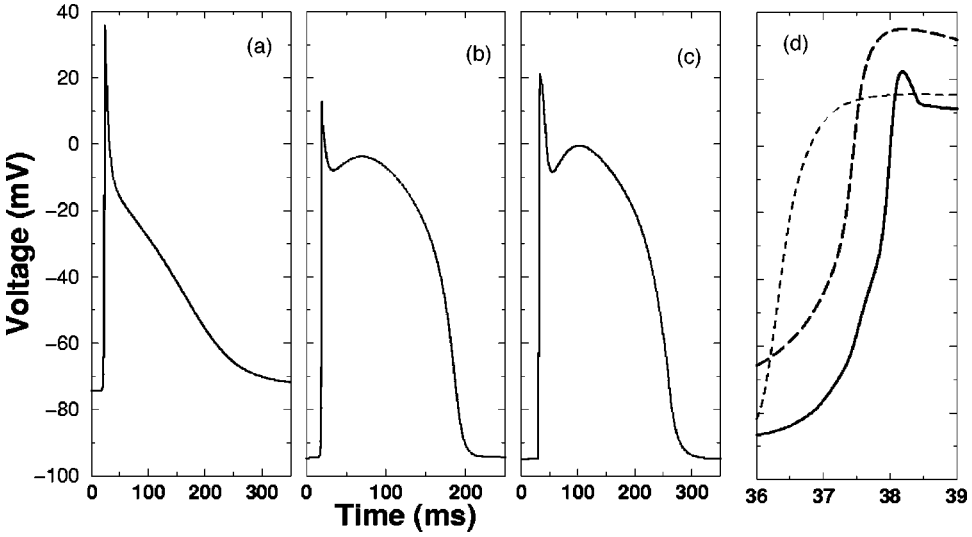

FIG. 3. Representative action potentials as measured in uniform cables from (a) the Nygren *et al.* human atrial model (Ref. 38), (b) the Fox *et al.* canine ventricular model (Ref. 39), and (c) the phenomenological ionic model in Ref. 12 with parameters to reproduce canine epicardial cells. Note that the Fox *et al.* model has a faster upstroke than the phenomenological model (values of $dV/dt_{\max}$ are 270 and 161 V/s, respectively). (d) The upstrokes corresponding to the models shown in (a) (long dashes), (b) (solid), and (c) (dashes). Models with different values of $dV/dt_{\max}$ are used to show its effect on the accuracy of the solutions obtained using the phase-field method (see Fig. 5).

using a variety of models. The upstrokes of the three models are shown in Fig. 3(d), and the values of $dV/dt_{\max}$ are 106, 270, and 161 V/s for the Nygren *et al.*, Fox *et al.*, and phenomenological canine epicardial models, respectively. Note that the maximum upstroke velocity is higher at any physical boundary with a no-flux boundary condition. In this case, the values of $dV/dt_{\max}$ at the boundary are 193, 368, and 237 V/s for the Nygren *et al.*, Fox *et al.*, and phenomenological canine epicardial models, respectively.

III. APPLICATION TO SAMPLE GEOMETRIES

A. One-dimensional cable

To illustrate the phase-field method and quantify its accuracy, we first apply it to a one-dimensional cable with zero-flux boundary conditions imposed by the phase field. A 5 cm long cable was embedded in a longer cable of length 6 cm and the middle of the domain was briefly excited to initiate two waves propagating toward the two ends of the cable. Figure 4 shows the resulting membrane potential V for a range of times during the depolarization (a) and repolarization (b). For comparison, the simulation results using a standard second-order-accurate finite-difference implementation of the boundary conditions are plotted as a solid line. Figure 4(c) shows the action potential at the right boundary using finite differences (solid) and the phase-field method (dotted). The error in the maximum upstroke velocity $dV/dt_{\max}$ using the phase-field method is about 2%, as shown in Fig. 5(a).

Figure 5 quantifies the accuracy of the cable solution of the three models as a function of the control parameter ξ by measuring the relative error in the maximum upstroke velocity (a), the cumulative error in the action potential (b), and the relative error in action potential duration (c) at the boundary, where the errors are largest. As expected, the maximum errors decrease as ξ and, consequently, the width of the phase field decrease. For the value of ξ shown in Fig. 4(a), 0.015 cm, the relative error in the maximum upstroke velocity is less than 5% for all three models, and it is less than 10% for $\xi=0.025$ cm. The other two error quantities indicate deviations from the finite-difference action potential

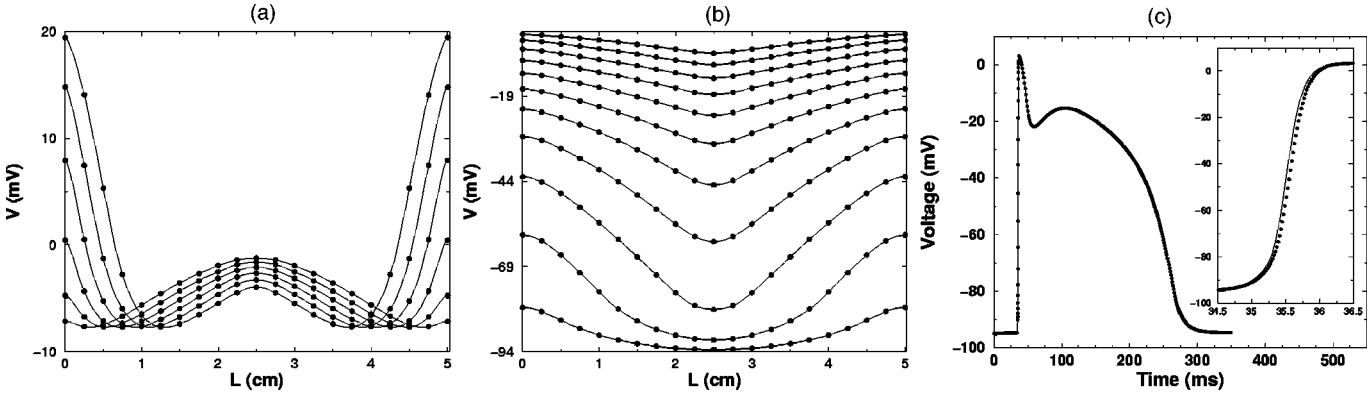

FIG. 4. Membrane potential distribution along a 5 cm-long cable at different times using the phase-field method with $\Delta x=0.025$ cm, $\Delta t=0.05$ ms, and $\xi=0.015$ cm (symbols) and using a standard zero-flux finite-difference code with the same discretization. The initial condition is a brief excitation at the center of the cable at $t=0$. This produces a symmetric excitation that propagates to the edges. (a) Voltage distribution during depolarization (all voltage values are >-10 mV). Initial time is $t=40$ ms, final time is $t=58$ ms, and the voltage distribution is plotted every 3 ms. (b) Voltage distribution during repolarization (all voltage values are <0 mV). Initial time is $t=110$ ms, final time is $t=275$ ms, and the voltage profile is plotted every 15 ms. (c) Comparison of action potentials at the boundary using finite differences (solid) and the phase-field method (dotted), with the two upstrokes highlighted in the inset. The phenomenological model is used.

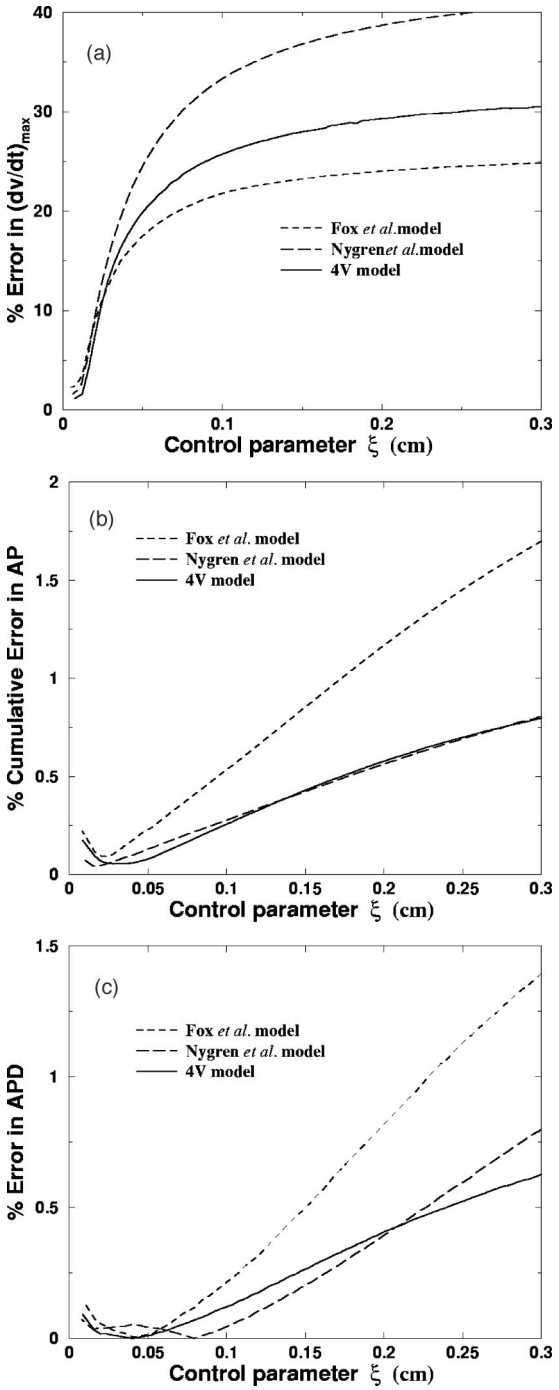

FIG. 5. (a) Relative error in the maximum upstroke velocity $(dV/dt)_{\max}$ as a function of the phase field width ξ for one-dimensional cable simulations as shown in Fig. 4 for the Fox *et al.* (short dashes), Nygren *et al.* (long dashes), and phenomenological (solid) models. Note that for the values of ξ used throughout this paper, the relative error is less than 10%. (b) Cumulative error in action potential for the same cases. The cumulative error is obtained by computing the absolute error in voltage over the time course of one action potential and then computing the ratio of the area under that curve to the area under the curve of the action potential calculated with the finite difference code. (c) Relative error in action potential duration for the same cases. In all cases, $\Delta x = 0.025$ cm and $\Delta t = 0.05$ ms. Slight increases in error can be observed for the smallest values of ξ because for these values the interface is very steep and is not adequately resolved by the fixed Δx used.

shape, and both errors rise steadily as ξ is increased but are significantly smaller than the error in maximum upstroke velocity. This is logical when one considers Eqs. (7) and (8): During the upstroke phase of the action potential, the right-hand side of Eq. (7) is large and the prefactor F in Eq. (8) is maximal. However, since this only occurs during a very small time interval, the error in quantities measured over the entire action potential are much smaller. We note that the error becomes large when the width of the interface becomes small relative to the the spatial resolution Δx (see Fig. 4).

B. Two-dimensional irregular tissue geometries

In two dimensions, it is useful to test the accuracy of the method for nontrivial geometries that can be solved using both a standard finite-difference code with the no-flux boundary condition applied at a sharp boundary and the phase-field method discretized with finite differences on a two-dimensional lattice. For isotropic tissue, an annular geometry with no-flux boundary conditions can be solved easily using finite differences after transforming Eq. (1) to polar coordinates as follows:

$$\frac{\partial V}{\partial t} = D\left[\frac{1}{\rho}\frac{\partial}{\partial \rho}\rho\frac{\partial V}{\partial \rho} + \frac{1}{\rho^2}\frac{\partial^2 V}{\partial^2 \rho}\right] - \frac{I_{\text{ion}}}{C_m}. \tag{12}$$

Figure 6 shows propagation in a quarter-annulus with an outer radius of 5 cm and an inner radius of 1.5 cm. The phase-field algorithm is implemented on a 200×200 square grid with a grid spacing of $\Delta x = 0.025$ cm. The tissue was briefly stimulated in the middle of the tissue and snapshots of the color-coded membrane potential are shown. A comparison of phase-field and finite-difference simulations in polar coordinates is shown in Fig. 6(e), where the contour $V = -60$ mV of the wave front is plotted at different times for the phase field (symbols) and for the finite-difference algorithm (solid lines). The same geometry is shown in Fig. 6(a), but in this case the excitation was initiated from the lower right corner. Agreement between wave front velocity in the two methods is very good in both cases, with less than 1% difference using the phase-field algorithm. The precise difference in the two methods depends slightly on the location within the tissue due to the fact that the polar coordinate discretization leads to a nonuniform grid spacing relative to a Cartesian grid because the grid spacing on the inner radius of the annulus is smaller than the grid spacing on the outer radius.

To make the geometry more complex in Cartesian coordinates, a quarter-annulus with an irregular-shaped hole can be used, as shown in Fig. 7(b). Note that despite its complex shape, the boundaries of this hole can be specified exactly in polar coordinates. As before, the wave front velocity obtained using the phase-field algorithm matches that obtained using the polar finite-difference algorithm within 1%. Furthermore, we have verified that an activation in the phase-field interface cannot stimulate the computational domain.

Because cardiac tissue is highly anisotropic, with propagation being two to three times faster along muscle fibers than across them, it is important to establish the accuracy of the phase-field method for domains with anisotropic conduction. Figure 7(c) shows a square containing a hole with fibers at an angle of $-53°$ relative to the vertical axis, a domain in which no-flux conditions can be implemented for all boundaries using finite differences. Excellent agreement is obtained

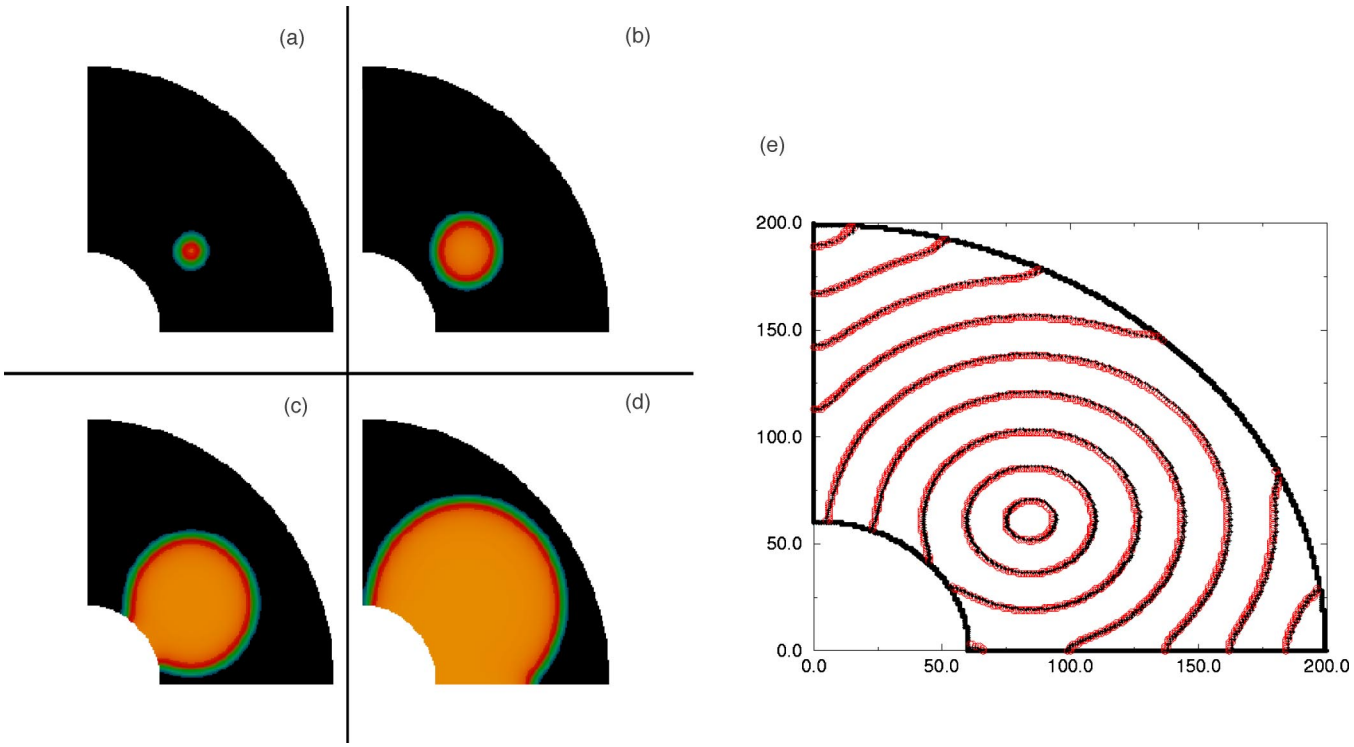

FIG. 6. (Color online). Propagation of a point stimulus applied off-center in a quarter-annulus. (a)–(d) Electrical excitation (orange) propagating into quiescent tissue (black) at times $t=10$, 20, 35, and 50 ms, respectively. (e) Comparison of wave front contours at 10 ms intervals for the solution using the phase-field method in Cartesian coordinates (red, symbols) and the reference solution using polar coordinates (black, solid). Grid spacings are $\Delta x=\Delta r=0.025$ cm and $\Delta\phi=0.007\,85$ or 0.45°, with $\xi=0.025$ cm.

between the phase-field and reference solutions for values of $\xi<0.03$ cm, as can be seen in Fig. 8. The relative error in the wave front velocity is below 10% over this range of ξ.

To summarize, in one- and two-dimensional regular and irregular domains with and without fiber anisotropy, the phase-field method yields accurate results for both the maximum upstroke velocity and the propagation speed.

IV. APPLICATION TO ANATOMICAL MODELS IN THREE DIMENSIONS

Having demonstrated the convergence of the phase field method in one- and two-dimensional domains, we now illustrate its application to more complex anatomical structures in three dimensions. Two of the data sets used here have been obtained by manually subdividing ventricles of animals (canine[19] and rabbit[20]) into thin slices, recording the fiber orientation and geometry throughout the slices, and reconstructing the original anatomy into a finite element model in prolate spheroidal coordinates following a computational procedure developed by Nielsen *et al.*[19] We also use a model of human atria that was originally digitized and reconstructed using finite elements.[24] For the simulations included here using the phase-field method, the finite-element models, including fiber orientation data for the two ventricular models, were interpolated and mapped onto a regular Cartesian grid with a grid spacing of 0.025 cm. The structure was then embedded in a computational box slightly larger than the structure, and the phase field was computed following Eq. (3) using $\xi=0.025$ cm. Note that because the phase field creates additional computational points near the surface, it is necessary to determine fiber orientation values at these points as explained in Sec. II. Other details of the fiber implementation are given in Appendix B.

Figure 9(a) shows complex behavior resulting from a scroll wave in the rabbit ventricular geometry using the Fenton–Karma three-variable model[12] with parameters adjusted to reproduce the electrophysiological effects of the electromechanical uncoupling agent cytochalasin-D in rabbit.[42] The computational nodes with $\phi>10^{-4}$ fill 30% of a $138\times130\times152$ box, and an anisotropy ratio of 5:1 is used ($D_{\text{parallel}}/D_{\text{perpendicular}}=0.001/0.0002$). Figure 9(b) shows a series of eight slabs for the same simulation 200 ms later to illustrate the irregular electrical activity in the interior. The scroll wave can be seen propagating around both ventricles and across the septum. One second of simulation time takes approximately 1.5 hours on a single 667 GHz Alpha processor.

Figure 9(c) shows simple propagation in the larger canine ventricular model, where computational nodes with $\phi>10^{-4}$ occupy 26% of a $400\times320\times320$ box. In this case, we have incorporated a simple Purkinje network to ensure a realistic activation sequence, similar to that detailed by Durrer *et al.*[43] In addition, the phenomenological model used includes three variations to represent endocardial, epicardial, and midmyocardial ventricular cells, which are distributed throughout the ventricular wall.[40] The midmyocardial cells can be observed in the interior of the wall where higher voltages, related to prolonged action potentials, are present. A typical simulation of 150 ms of electrical activity takes approximately 15 minutes using 32 1 GHz Alpha processors.

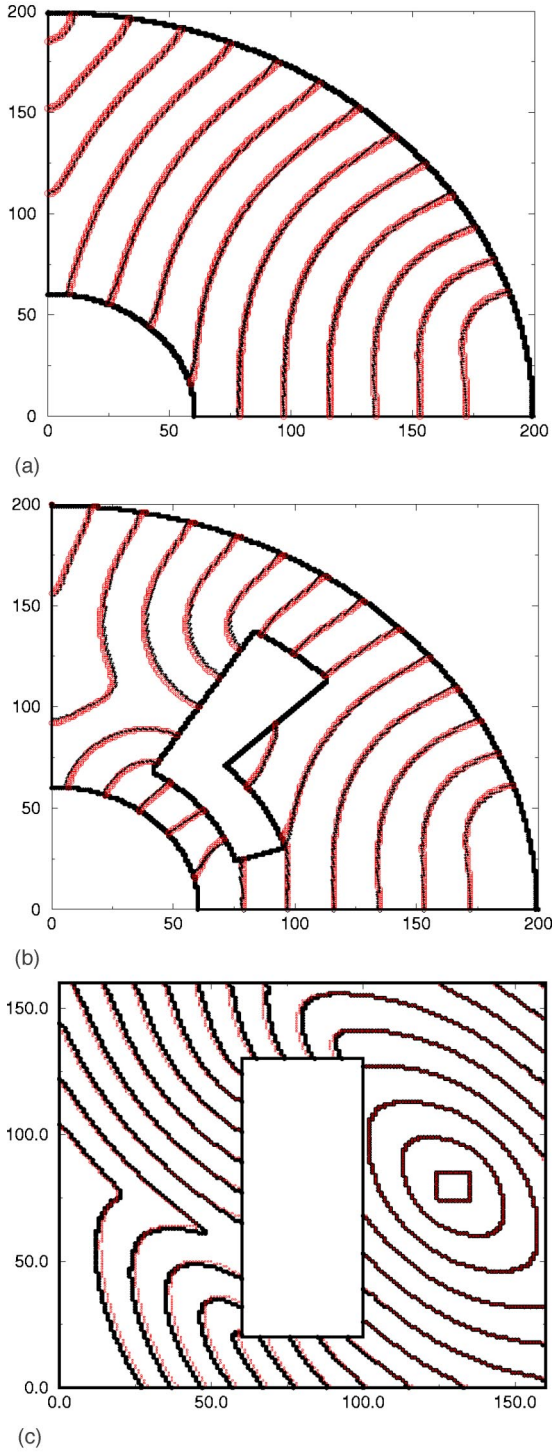

FIG. 7. (Color online). Propagation of a point stimulus applied (a) to the lower right corner of a quarter-annulus, (b) to the lower right corner of a quarter-annulus with a hole, and (c) near the right edge of an anisotropic square domain with a hole. Wave front contours are shown at 10 ms intervals for the solution using the phase-field method (red, symbols) and for the reference solution using finite differences (black, solid). Reference solutions are obtained using polar coordinates in (a) and (b) and using standard finite differences in (c). Note that the contours are normal to all the boundaries for both solutions in (a) and (b). The ratio of diffusion constants parallel and perpendicular to the fibers in (c) is $D_{\text{parallel}}/D_{\text{perpendicular}}=0.001/0.0002=5$ and the fiber angle is $-53°$. Grid spacings are $\Delta x=\Delta r=0.025$ cm and $\Delta\phi=0.007\,85$ or $0.45°$ with $\xi=0.025$ cm for (a) and (b), while for (c) the grid spacing is $\Delta x=0.025$ cm with $\Delta t=0.5$ ms and $\xi=0.025$ cm.

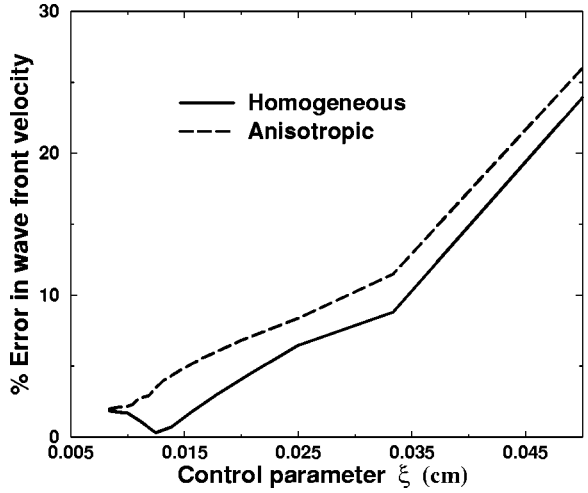

FIG. 8. Maximum relative error in propagation velocity in the domain shown in Fig. 7(c) as a function of the ξ, the width of the phase field. For values of ξ below 0.03 cm, the error is less than 10%. The inclusion of anisotropy increases the error by 2%–4% compared to an isotropic simulation for nearly all values of ξ tested.

A final example of a still more complex geometry is shown in Fig. 9(d). Here, the human atrial structure is used in conjunction with the Nygren human atrial cell model.[38] In this geometry, computational nodes with $\phi>10^{-4}$ occupy 14% of a $320\times300\times230$ box. A scroll wave rotating in the thin wall of the left atrium appears as a spiral, which propagates into the right atrium via interatrial connections. Complicated patterns can result even from simple propagation due to the presence of anatomical structures such as blood vessels and valve annuli. With this structure, a simulation of 500 ms of electrical activity using the Nygren *et al.* model requires the use of distributed memory and takes approximately 2.5 hours using 64 1 GHz Alpha processors.

A significant advantage of using the phase-field method is that for all of these different geometries, the only code change required is the specification of a different file representing the phase field and the fibers of the desired anatomy. Whereas finite-element models with irregular elements necessitate complicated grid generation procedures, only a simple Cartesian grid structure is required, which then is used to generate a phase-field interface. This makes the phase-field method efficient, flexible, and practical for use with a variety of complex cardiac geometries.

V. CONCLUSION

We have presented a new algorithm for implementing no-flux boundary conditions in irregular domains, including anatomical cardiac models. The phase-field method uses an auxiliary field to distinguish between the interior and the exterior of cardiac tissue. The no-flux boundary condition is recovered formally in the limit where the width of the diffuse interface between these two regions approaches zero. In practice, this boundary condition is accurately modeled when this width is small relative to the width of the activation wavefront, which is the smallest length scale in the wave propagation problem. Even though we have used simple finite differences to discretize the partial differential equations

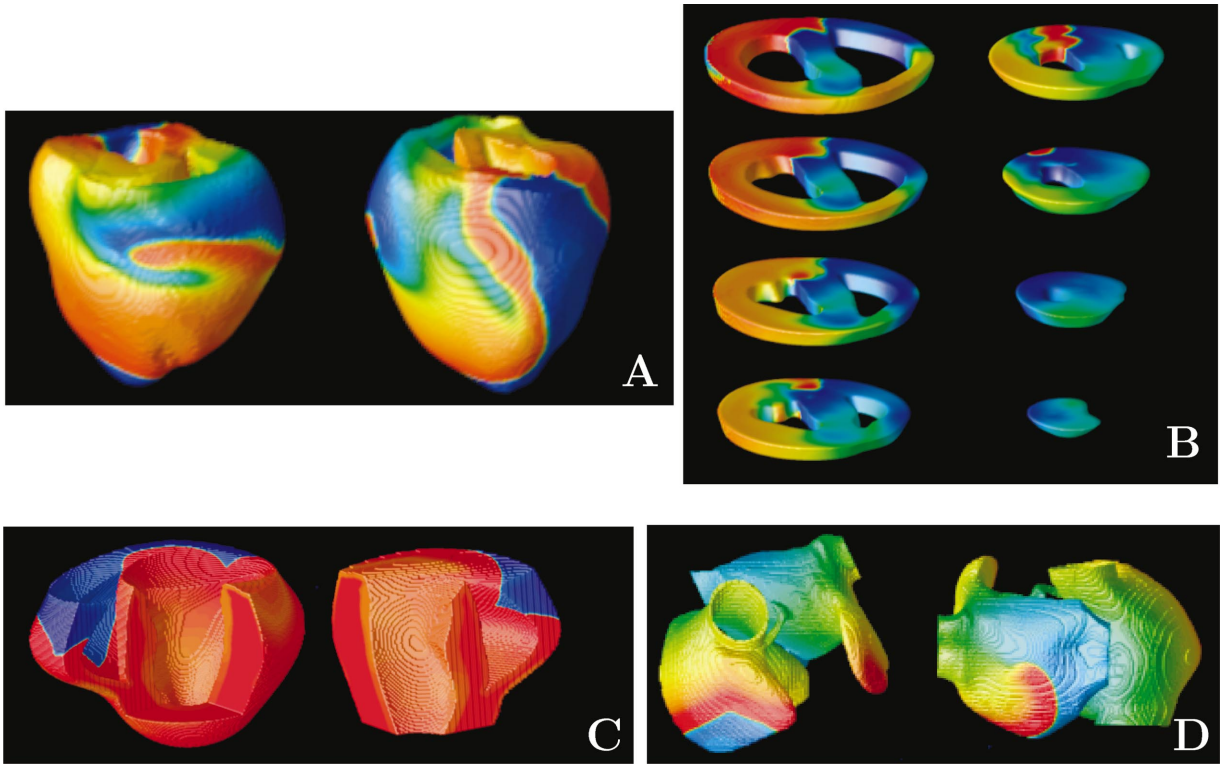

FIG. 9. (Color). Example simulations using the phase-field method in complex cardiac geometries. (a) Single scroll wave in the rabbit ventricular model. The left and right images show posterior and anterior views, respectively. (b) Slabs of the rabbit ventricles during scroll wave propagation (posterior view). The slabs are perpendicular to the apex-base axis and proceed toward the apex. (c) Propagation of an electrical wave in the canine ventricles 55 ms after a stimulus along a simulated Purkinje network. The left image shows an anterior view of the ventricles with a small portion cut out to allow the endocardium to be seen. The cut-out view on the right shows the anterior endocardium. (d) Two views of a spiral wave in the anatomical model of the human atria. The Nygren *et al.* model of human atrial cells is used. Electrical potential is color-coded with red corresponding to strongly depolarized tissue and blue corresponding to repolarized tissue. In all cases, grid spacing is 0.025 cm, and the phase-field control parameter ξ is 0.025 cm. Time steps are 0.02 ms for (a) and (b), 0.05 ms for (c), and 0.015 ms for (d).

both in space and in time, the phase-field method, in principle, is independent of the integration scheme.[37] We have provided a number of examples quantifying the method's accuracy using various nontrivial test geometries and demonstrating its applicability to more complex anatomical models of the heart. Furthermore, we have shown the feasibility of the method for several ionic models of differing levels of physiological realism. These examples demonstrate that the phase-field method is highly accurate in both isotropic and anisotropic domains while retaining simplicity in concept and ease of implementation. Systematic studies using various anatomical geometries are currently under way.

We anticipate that this method will find increasing use to describe cardiac geometries. The availability of new methods for obtaining the necessary anatomical data such as diffusion tensor MRI[44,45] has made it easier and faster to obtain geometrical descriptions of cardiac structures. The phase-field algorithm offers a quick, practical method for simulating electrical activity using new anatomical models with a smoother representation of the complex boundaries than traditional stairstep approaches but without the need for the complex and time-consuming task of grid generation for a finite-element model with irregular grids. In addition, the phase-field method does not require any changes when using new geometries other than specifying the appropriate input geometry file and surrounding box size; no changes need to be made to the evolution equations or memory handling.

Although we have considered only the simplest situation where the heart is electrically isolated, it should be possible to extend the method to bidomain models (for a review see, e.g., Ref. 46) with the heart embedded in a conducting medium by exploiting the property that the phase field interpolates smoothly between the electrical properties of different regions.

Perhaps the most exciting future prospect for this method is to couple electrical wave propagation and mechanical function. The phase-field method appears ideally suited for this extension given its successful history of handling complex moving boundary problems. Computational constraints associated with finite-element techniques currently limit efforts to study such models (for a review see, e.g., Ref. 47). Given the ease of implementation and the speed of our algorithm, we believe that the phase-field method can provide an attractive and computationally feasible alternative. As a result of the coupling of the cellular calcium dynamics to the contraction of the myofibers, the heart boundaries are no longer stationary and the phase field becomes a dynamic variable. This extension should take into account the force generation along with the appropriate pressure conditions at the boundaries.

ACKNOWLEDGMENTS

We gratefully acknowledge the hospitality of the Aspen Center for Physics where part of this research was performed. This research was facilitated through an allocation of advanced computing resources by the National Computational Science Alliance, through the support of the National Science Foundation, and the computations were performed in part on the National Science Foundation Terascale Computing System at the Pittsburgh Supercomputing Center. We acknowledge the National Biomedical Computation Resource (National Institutes of Health Grant No. P41 RR-08605). This research was supported in part by National Science Foundation Grants No. PHY99-07949 and No. 0320865 (F.H.F. and E.M.C.), by NIH Grant No. 5 F32 HL073604-02 (E.M.C.), by the NSF-sponsored Center for Theoretical Biological Physics (Grants No. PHY-0216576 and No. 0225630) (W.-J.R.), and by NIH Grant No. HL075515-01 (W.-J.R.). A.K. acknowledges support of NIH Grant No. P50-HL52319.

APPENDIX A

As explained in the main text, the expression for the voltage at gridpoint i,j,k at time step n, $V^n(i,j,k)$, can be written as a weighted sum of the voltages at its 18 nearest and next-nearest neighbors and the voltage at the gridpoint itself. Using an explicit time-stepping algorithm with time step Δt and grid spacing Δx, the voltage $V^{n+1}(i,j,k)$ at time step $n+1$ can thus be expressed as

$$\begin{aligned} V^{n+1}(i,j,k) = V^n(i,j,k) + \frac{\Delta t}{\Delta x^2}[&F^{i,j,k}(i,j,k)V^n(i,j,k) \\ &+ F^{i,j,k}(i+1,j,k)V^n(i+1,j,k) + \cdots \\ &+ F^{i,j,k}(i+1,j+1,k)V^n(i+1,j+1,k) + \cdots] \end{aligned} \tag{A1}$$

where we have, for simplicity, omitted the current term. The dots in this expression represent terms obtained by changing +1 into −1 and/or by permutation over i, j, and k. Thus, the first set of dots represents five additional terms, while the second set of dots represents eleven additional terms. The weights F appearing in this expression can be written as follows:

$$\begin{aligned} F^{i,j,k}(i,j,k) = -[&D_\perp(\phi_{i+1/2} + \phi_{i-1/2} + \phi_{j+1/2} + \phi_{j-1/2} \\ &+ \phi_{k+1/2} + \phi_{k-1/2}) + D_d(\phi_{i+1/2}(f^x_{i+1/2})^2 \\ &+ \phi_{j+1/2}(f^y_{j+1/2})^2 + \phi_{k+1/2}(f^z_{k+1/2})^2 \\ &+ \phi_{i-1/2}(f^x_{i-1/2})^2 + \phi_{j-1/2}(f^y_{j-1/2})^2 \\ &+ \phi_{k-1/2}(f^z_{k-1/2})^2)], \end{aligned} \tag{A2}$$

$$\begin{aligned} F^{i,j,k}(i+1,j,k) = D_\perp\phi_{i+1/2} + \frac{D_d}{4}(&4\phi_{i+1/2}(f^x_{i+1/2})^2 \\ &+ \phi_{j+1/2}f^x_{j+1/2}f^y_{j+1/2} + \phi_{k+1/2}f^x_{k+1/2}f^z_{k+1/2} \\ &- \phi_{j-1/2}f^x_{j-1/2}f^y_{j-1/2} - \phi_{k-1/2}f^x_{k-1/2}f^z_{k-1/2}), \end{aligned} \tag{A3}$$

$$\begin{aligned} F^{i,j,k}(i+1,j+1,k) = \frac{D_d}{4}(&\phi_{i+1/2}f^x_{i+1/2}f^y_{i+1/2} \\ &+ \phi_{j+1/2}f^x_{j+1/2}f^y_{j+1/2}) \end{aligned} \tag{A4}$$

where $D_\parallel$ and $D_\perp$ are the diffusion constants parallel and perpendicular to the fiber, respectively, and $D_d = D_\parallel - D_\perp$. Along with similar expressions for the other terms in Eqs. (A2)–(A4), we have used the following notation:

$$\phi_{i+1/2} = \tfrac{1}{2}(\phi(i,j,k) + \phi(i+1,j,k)) \tag{A5}$$

and

$$f^x_{i+1/2} = \tfrac{1}{2}(f^x(i,j,k) + f^x(i+1,j,k)) \tag{A6}$$

where $f^x(i,j,k)$ represents the x-component of the fiber vector $\mathbf{f}$ at grid position i,j,k.

APPENDIX B

To compute the elements of the conductivity tensor given the fiber orientation at the Cartesian gridpoint we employ the same technique as Ref. 21. The fiber orientation at each point is given by a unit vector $\mathbf{f}$. This defines a local coordinate frame in which the conductivity tensor is diagonal:

$$\tilde{\mathbf{D}} = \begin{pmatrix} D_\parallel & 0 & 0 \\ 0 & D_\perp & 0 \\ 0 & 0 & D_\perp \end{pmatrix}. \tag{B1}$$

Here, $D_\parallel$ is the diffusion constant for propagation parallel to the fiber and $D_\perp$ is the diffusion constant for propagation perpendicular to the fibers (taken to be the same in both perpendicular directions). In the Cartesian coordinate frame of our heart this tensor is only diagonal if the fiber orientation is parallel to one of the axes. Thus, to find a representation $\mathbf{D}$ of the tensor in our coordinate frame we need to find the transformation matrices $\mathbf{A}$ and $\mathbf{A^T}$ such that

$$\mathbf{D} = \mathbf{A}\tilde{\mathbf{D}}\mathbf{A^T}. \tag{B2}$$

The matrix $\mathbf{A}$ can be obtained by writing out the involved rotations explicitly. An alternative method uses the fact that $\mathbf{f}$ and the two vectors orthogonal to it, $\mathbf{g}$ and $\mathbf{h}$, are eigenvectors of $\mathbf{D}$ with eigenvalues $D_\parallel$ and $D_\perp$. Thus, $\mathbf{A}$ is an orthogonal matrix of the form $\mathbf{A}=(\mathbf{f},\mathbf{g},\mathbf{h})$, and $\mathbf{D}$ can be written, using Eq. (B2), as

$$\mathbf{D} = D_\parallel\mathbf{f}\mathbf{f^T} + \mathbf{D}_\perp(\mathbf{g}\mathbf{g^T} + \mathbf{h}\mathbf{h^T}). \tag{B3}$$

Finally, making use of the fact that $\mathbf{A}\mathbf{A^T}=\mathbf{I}$ we find

$$\mathbf{D} = D_\perp\mathbf{I} + (D_\parallel - D_\perp)\mathbf{f}\mathbf{f^T}, \tag{B4}$$

which shows that the conductivity matrix can be expressed in terms of only the fiber orientation vector $\mathbf{f}$.

[1] A. T. Winfree, *When Time Breaks Down: The Three-dimensional Dynamics of Electrochemical Waves and Cardiac Arrhythmias* (Princeton University Press, Princeton, NJ, 1987).

[2] D. W. Frazier, P. D. Wolf, J. M. Wharton, A. S. Tang, W. M. Smith, and R. E. Ideker, "Stimulus-induced critical point. Mechanism for electrical initiation of reentry in normal canine myocardium," J. Clin. Invest. **3**, 1039–1052 (1989).

[3] J. M. Davidenko, A. V. Pertsov, R. Salomonsz, W. Baxter, and J. Jalife,

"Stationary and drifting spiral waves of excitation in isolated cardiac muscle," Nature (London) **355**, 349–351 (1992).
[4]R. A. Gray, A. M. Pertsov, and J. Jalife, "Spatial and temporal organization during cardiac fibrillation," Nature (London) **392**, 75–78 (1998).
[5]F. X. Witkowski, L. J. Leon, P. A. Penkoske, W. R. Giles, M. L. Spano, W. L. Ditto, and A. T. Winfree, "Spatiotemporal evolution of ventricular fibrillation," Nature (London) **392**, 78–82 (1998).
[6]M. Courtemanche and A. T. Winfree, "Re-entrant rotating waves in a Beeler–Reuter based model of two-dimensional cardiac electrical activity," Int. J. Bifurcation Chaos Appl. Sci. Eng. **1**, 431–444 (1991).
[7]A. Karma, "Spiral breakup in model equations of action potential propagation in cardiac tissue," Phys. Rev. Lett. **71**, 1103–1106 (1993).
[8]V. N. Biktashev, A. V. Holden, and H. Zhang, "Tension of organized filaments of scroll waves," Philos. Trans. R. Soc. London, Ser. A **347**, 611–630 (1994).
[9]F. H. Fenton, E. M. Cherry, H. M. Hastings, and S. J. Evans, "Multiple mechanisms of spiral wave breakup in a model of cardiac electrical activity," Chaos **12**, 852–892 (2002).
[10]O. Berenfeld and A. M. Pertsov, "Dynamics of intramural scroll waves in three-dimensional continuous myocardium with rotational anisotropy," J. Theor. Biol. **199**, 383–394 (1999).
[11]A. Panfilov and J. Keener, "Re-entry in three-dimensional FitzHugh–Nagumo medium with rotational anisotropy," Physica D **84**, 545–552 (1995).
[12]F. Fenton and A. Karma, "Vortex dynamics in three-dimensional continuous myocardium with fiber rotation: Filament instability and fibrillation," Chaos **8**, 20–47 (1998).
[13]W.-J. Rappel, "Filament instability and rotational tissue anisotropy: A numerical study using detailed cardiac models," Chaos **11**, 71–80 (2001).
[14]J. M. Rogers, "Wave front fragmentation due to ventricular geometry in a model of the rabbit heart," Chaos **12**, 779–787 (2002).
[15]W. Reinboldt, J. A. Abildkov, R. S. Ledley, and A. E. Oestreich, "Simulation of the ventricles of the heart," *Proceedings of the 16th Annual Conference on Engineering in Medicine and Biology* (1963), pp. 32–33.
[16]M. Okajima, T. Fujino, T. Kobayashi, and K. Yamada, "Computer simulation of the propagation process in excitation of the ventricles," Circ. Res. **23**, 203–211 (1968).
[17]M. Lorange and R. M. Gulrajani, "Computer simulation of the Wolff–Parkinson–White preexcitation syndrome with a modified Miller–Geselowitz heart model," IEEE Trans. Biomed. Eng. **33**, 862–873 (1986).
[18]A. Yamanaka, K. Okazaki, S. Urushibara, M. Kawato, and R. Suzuki, "Reconstruction of electrocardiogram using ionic current models for heart muscles," Jpn. Heart J. **27**, 185–193 (1986).
[19]P. M. Nielsen, I. J. Le Grice, B. H. Smaill, and P. J. Hunter, "Mathematical model of geometry and fibrous structure of the heart," Am. J. Physiol. Heart Circ. Physiol. **260**, H1365–H1378 (1991).
[20]F. J. Vetter and A. D. McCulloch, "Three-dimensional analysis of regional cardiac function: a model of rabbit ventricular anatomy," Prog. Biophys. Mol. Biol. **69**, 157–183 (1998).
[21]A. V. Panfilov and J. P. Keener, "Re-entry in an anatomical model of the heart," Chaos, Solitons Fractals **5**, 681–689 (1995).
[22]J. M. Meunier, J. C. Eason, and N. A. Trayanova, "Termination of reentry by a long-lasting AC shock in a slice of canine heart: a computational study," J. Cardiovasc. Electrophysiol. **13**, 1253–1261 (2002).
[23]F. Xie, Z. Qu, J. Yang, A. Baher, J. N. Weiss, and A. Garfinkel, "A simulation study of the effects of cardiac anatomy in ventricular fibrillation," J. Clin. Invest. **113**, 686–693 (2004).
[24]D. Harrild and C. Henriquez, "A computer model of normal conduction in the human atria," Circ. Res. **87**, E25–E36 (2000).
[25]A. Fogelson and J. P. Keener, "Immersed interface methods for Neumann and related problems in two and three dimensions," SIAM J. Sci. Comput. (USA) **22**, 1630–1654 (2001).
[26]M. Dumett and J. P. Keener, "A numerical method for solving anisotropic elliptic boundary value problems in 3D," SIAM J. Sci. Comput. (USA) **25**, 348–367 (2003).
[27]F. J. Vetter and A. D. McCulloch, "Three-dimensional stress and strain in passive rabbit left ventricle: a model study," Ann. Biomed. Eng. **28**, 781–792 (2000).
[28]A. Karma and W.-J. Rappel, "Quantitative phase-field modeling of dendritic growth in two and three dimensions," Phys. Rev. E **57**, 4323–4349 (1998).
[29]R. Folch, J. Casademunt, A. Hernandez-Machado, and L. Ramirez-Piscina, "Phase-field model for Hele-Shaw flows with arbitrary viscosity contrast," Phys. Rev. E **60**, 1724–1733 (1999).
[30]I. S. Aranson, V. A. Kalatsky, and V. M. Vinokur, "Continuum field description of crack propagation," Phys. Rev. Lett. **85**, 118–121 (2000).
[31]A. Karma, D. A. Kessler, and H. Levine, "Phase-field model of mode III dynamic fracture," Phys. Rev. Lett. **87**, 045501 (2001).
[32]T. Biben and C. Misbah, "Tumbling of vesicles under shear flow within an advected-field approach," Phys. Rev. E **67**, 031908 (2003).
[33]J. Kockelkoren, H. Levine, and W. J. Rappel, "Computational approach for modeling intra and extracellular dynamics," Phys. Rev. E **68**, 037702 (2003).
[34]R. Plonsey and R. C. Barr, *Bioelectricity: A Quantitative Approach* (Plenum, New York, 1988).
[35]A. V. Panfilov and J. P. Keener, "Generation of reentry in anisotropic myocardium," J. Cardiovasc. Electrophysiol. **4**, 412–421 (1993).
[36]D. Streeter, "Gross morphology and fiber geometry in the heart," in *Handbook of Physiology*, edited by R. Berne (American Physiological Society, Bethesda, 1979), pp. 61–112.
[37]A. Bueno-Orovio, V. M. Pérez-García, and F. H. Fenton, "Spectral methods for partial differential equations in irregular domains: The spectral smoothed boundary method" (in preparation).
[38]A. Nygren, C. Fiset, L. Firek, J. W. Clark, D. S. Lindblad, R. B. Clark, and W. R. Giles, "Mathematical model of an adult human atrial cell: the role of K+ currents in repolarization," Circ. Res. **82**, 63–81 (1998).
[39]J. J. Fox, J. L. McHarg, and R. F. Gilmour, "Ionic mechanism of electrical alternans," Am. J. Physiol. Heart Circ. Physiol. **282**, H516–H530 (2002).
[40]E. M. Cherry, W.-J. Rappel, S. J. Evans, and F. Fenton, "Effects of wall heterogeneity in an anatomically realistic model of canine ventricles: A simulation study," PACE **26**, 1109–1109 (2003).
[41]F. H. Fenton, E. M. Cherry, J. R. Ehrlich, S. Nattel, and S. J. Evans, "A simulation study of atrial fibrillation initiation: Differences in resting membrane potential can produce spontaneous activations at the pulmonary vein-left atrial junction," Heart Rhythm **1**, S187–S188 (2004).
[42]F. H. Fenton, E. M. Cherry, I. Banville, R. A. Gray, H. M. Hastings, A. Karma, and S. J. Evans, "Validation of realistic 3D computer models of ventricular arrhythmias with optical mapping experiments," Pacing Clin. Electrophysiol. **24** (Part II), 538 (2002).
[43]D. Durrer, R. T. van Dan, G. E. Freud, M. J. Janse, F. L. Meijler, and R. C. Arzbaecher, "Total excitation of the isolated human heart," Circulation **41**, 899–912 (1970).
[44]D. F. Scollan, A. Holmes, J. Zhang, and R. L. Winslow, "Reconstruction of cardiac ventricular geometry and fiber orientation using magnetic resonance imaging," Ann. Biomed. Eng. **28**, 934–944 (2000).
[45]F. B. Sachse, C. Henriquez, G. Seemann, C. Riedel, C. D. Werner, R. C. Penland, B. Davis, and E. Hsu, "Modeling of fiber orientation in the ventricular myocardium with mr diffusion imaging," Comput. Cardiol. **28**, 617–620 (2001).
[46]C. S. Henriquez, "Simulating the electrical behavior of cardiac tissue using the bidomain model," Crit. Rev. Biomed. Eng. **21**, 1–77 (1993).
[47]P. J. Hunter, A. J. Pullan, and B. H. Smaill, "Modeling total heart function," Annu. Rev. Biomed. Eng. **5**, 147–177 (2003).